Where Q represents the relative spectral response of the detector, G_{amp} is the amplifier gain and V_{offset} is the offset adjustment of the amplifier.

The amplification stages are also source of uncertainty due to possible non-linear characteristic of the gain curve (harmonic distortion of the signal) and the introduced noise. Moreover also the detector spectral response affects systematically the sensitivity along the measured spectral range and it should be characterized together with the amplification parameters according to the analysed sample.

The amplified output voltage is then digitalized with the A/D converter embedded in the FV300 scan head or with another A/D acquisition board. The digitalized data converted through the FV300 scan head converter are recorded in the computer hard disk using the Olympus Fluoview software that reconstructs the image managing the FV300 scan unit. The A/D conversion is also source of uncertainty due to the quantization noise introduced and to the discretization of the intensity in 1024 levels. The integration time related to each pixel (also called dwell pixel time) that can be adjusted choosing among three predefined values using the Fluoview software installed on our system, is also a source of uncertainty because the signal-to-noise ratio changes in its function.

Another common main source of uncertainty is related to the image processing with specific algorithms in order to enhance image quality, to perform three-dimensional reconstructions or to extract specific information from the acquired images. The process method used to implement the algorithms could dramatically affect the measured values, due to different reasons like the image quality, the pixels intensity distribution, etc., together with the algorithms themselves.

For such regards TPEF and SHG microscopy techniques it is possible to use a similar approach to identify the sources of uncertainty of the measure, separating the sources of uncertainty related to the sample type from those related to the modules that compose all the measurement system.

When TPEF microscopy technique is used, the measure of the fluorescence intensity is related to the amount of a target molecule present in the sample. Usually fluorophores are linked with specific molecules that allow selective binding of a specific biomolecule in the sample. The process of fluorophore modification that allows selective biomolecular binding is called fluorophore bio-conjugation. The bio-conjugation can be done in a way that a single fluorophore binds with a single biomolecule, or more fluorophores could bind with a single biomolecule or a fluorophores could bind more biomolecules. Moreover the efficiency of bio-conjugation can vary depending by the sample and by the method adopted to stain the sample. The bio-conjugation mechanism is thus an important source of uncertainty in the measure of the amount of the target biomolecule in a sample, since it is not easy to quantify the bio-conjugation efficiency. Also the way the fluorophores are used could favourite some inherent drawbacks such as the fluorescent quenching (when the fluorescence intensity is reduced due to molecular collisions that increase when the fluorophore concentration is high) and the photo-bleaching (when the excitation intensity switches off the fluorophores also in a permanent way due to the excitation exposure time) that are both sources of uncertainty.

The type of fluorophore could add a source of uncertainty because of its fluorescence mechanism that plays a fundamental role in the fluorescence measurement. Not all the fluorophores present in the focal volume are excited properly and not all the excited fluorophores emit a light radiation due to non-radiative recombination phenomena.

The TPEF intensity can be expressed as:

$$I_{TPEF} = I_{ex}^2 N \Omega_{bc} \Omega_q \Omega_{pb} \gamma_{TPEF} \delta_{TPE} \quad (34)$$

Where I_{ex} is the intensity of the excitation source, N is the number of fluorophores, Ω_{bc} is the bio-conjugation factor that condiders the average number of fluorophores per biomolecule, Ω_q is a factor that takes into account quenching attenuation, Ω_{pb} is a factor that considers photo-bleaching attenuation, γ_{TPEF} represents the emission efficiency and δ_{TPE} is the two-photon cross-section of the fluorophore.

As for CARS microscopy, the attenuation factors due to the optical system and the optical characteristic of the sample must be considered also for TPEF microscopy. The excitation source intensity $I_{ex,0}$ is attenuated in function of the wavelength by a factor Ω_{ex} due to the optical components used to address and optimize the excitation source on the sample, such as mirrors, optical filters, iris, spatial filters and lenses. Considering also the attenuation due to the sample optical transmittance and to the optical components between the sample and the detector $\Omega_{tr,TPEF}$ and $\Omega_{tr,ex}$ (respectively for the generated TPEF signal end the excitation source), with the effect of the residual ambient light I_{amb} that can hit the sensor surface and a possible spectral overlap of two-photon excitation autofluorescence emitted by the sample $\Omega_{af} I_{af}$, the measured TPEF intensity at the detector surface could be expresses as:

$$I_{TPEF,det} = \Omega_{tr,TPEF} \Omega_{sp,TPEF} \left(\Omega_{sp,ex} \Omega_{ex} I_{ex,0}\right)^2 N \Omega_{bc} \Omega_q \Omega_{pb} \gamma_{TPEF} \delta_{TPE} + \Omega_{tr,ex} \Omega_{sp,ex} \Omega_{ex} I_{ex,0} + I_{amb} + \Omega_{af} I_{af} \quad (35)$$

Where $\Omega_{\mathrm{sp,TPEF}}$ and $\Omega_{\mathrm{sp,ex}}$ represent the attenuation factors due to the optical transmittance of the sample respectively for the generated TPEF signal end the excitation source.

The principle of the TPEF and SHG detection system is the same of that used for CARS microscopy thus eq. (33) could be applied also for TPEF microscopy substituting $V_{aS,det}$ and $I_{aS,det}$ with $V_{TPEF,det}$ and $I_{TPEF,det}$:

$$V_{TPEF,det} = I_{TPEF,det} Q G_{amp} + V_{offset} \quad (36)$$

The SHG microscopy allows imaging of molecules with non-centrosymmetric ordered structures and the SHG intensity is directly related to the number of this type of molecules present in the focal volume. Differently to TPEF that utilizes fluorophores to target specific molecules, SHG technique gives a chemical selectivity related to the nature of the target molecules similarly to CARS microscopy in a label-free way. From this point of view the part of uncertainty sources related to the preparation of the sample for staining is completely avoided since no staining is needed to have contrast with SHG microscopy (unless a SHG staining is used).

The SHG signal intensity is related to the effective second-order susceptibility of the material that is linearly linked with the amount of molecules and takes into account the polarization of the excitation source with respect to the spatial orientation of the excited molecule. These last two parameters are sources of uncertainty in SHG microscopy because could change the efficiency of frequency doubling conversion of the excitation signal.

Moreover the second-order susceptibility of the material contains also a non-resonant component that for simplicity has been neglected in this model. However like for CARS and TPEF microscopy uncertainty models, the effect of the two-photon autofluorescence emission of the target molecules has been considered. Starting from eq. (21) a source of uncertainty is also the refractive index variation into the sample together with the attenuation of the excitation source due to the optical components between the

source and the sample Ω_{ex} and the attenuation of both excitation source and generated source due to the sample transmittance respectively $\Omega_{\mathrm{sp,SHG}}$ and $\Omega_{\mathrm{sp,ex}}$. The SHG intensity can thus be expressed as:

$$I_{SHG} = \Omega_{\mathrm{sp,SHG}} \frac{2\omega^2 {\chi_{eff}^{(2)}}^2 l^2}{n_{2\omega} n_{\omega}^2 c^3 \epsilon_0} \left(\frac{\sin(\Delta k l/2)}{\Delta k l/2}\right)^2 \left(\Omega_{sp,ex}\Omega_{ex} I_{ex,0}\right)^2 \quad (37)$$

Considering also the attenuation due to the sample optical transmittance and to the optical components between the sample and the detector $\Omega_{tr,SHG}$ and $\Omega_{tr,ex}$ (respectively for the generated SHG signal end the excitation source), with the effect of the residual ambient light I_{amb} that can hit the sensor surface and a possible spectral overlap of two-photon excitation autofluorescence emitted by the sample $\Omega_{af} I_{af}$, the measured SHG intensity at the detector surface could be expresses as:

$$I_{SHG,det} = \Omega_{tr,SHG}\Omega_{sp,SHG}\left(\Omega_{sp,ex}\Omega_{ex} I_{ex,0}\right)^2 \frac{2\omega^2 {\chi_{eff}^{(2)}}^2 l^2}{n_{2\omega} n_{\omega}^2 c^3 \epsilon_0} \left(\frac{\sin(\Delta k l/2)}{\Delta k l/2}\right)^2 + \Omega_{tr,ex}\Omega_{sp,ex}\Omega_{ex} I_{ex,0} + I_{amb} + \Omega_{af} I_{af} \quad (38)$$

After being transduced by the detector and amplified by the electronic system the resulting output voltage similarly to eq. (33) and eq. (36) is then:

$$V_{SHG,det} = I_{SHG,det} Q G_{amp} + V_{offset} \quad (39)$$

The same considerations done for CARS microscopy can be done also for TPEF and SHG microscopy for such regards the A/D conversion and the image processing.

Conclusion

For such complex system it is not easy to evaluate experimentally each source of uncertainty contribution, above all those directly related to the type of sample. It is thus very important to have reference materials that can be used to calibrate the measurement system for specific experiments. During the realization of the CARS microscope a polystyrene slab, characterized using linear Raman microscopy, has been used as reference material to verify the agreement between the CARS spectroscopy measurements and the expected computed spectrum. This was really important to understand if the system was working properly and actually measuring CARS signal.

Reference materials with certified values of chemical composition and purity could be used to calibrate the microscope in terms of sensitivity and ability to perform quantitative analysis. These materials should be specifically chosen for the different techniques. For TPEF microscopy could be used mixtures with different certified concentrations of fluorophores, for SHG microscopy could be used mixtures with different concentration of non-centrosymmetric molecules, for CARS microscopy could be mixtures of species that allow a clear spectral separation between the target substance and the matrix/solvent chemical species.

Nowadays there are not reference materials with certified CARS spectra but the availability of these materials should be very important in order to calibrate the spectroscopy response of the system considering true CARS spectra. Deriving computationally CARS spectra from the linear Raman spectra databases, or vice versa linear Raman spectra from the CARS spectra, does not guarantee that a realistic approximation of the non-resonant background is considered, adding an important source of uncertainty.

Spatial characterization of the multimodal CARS microscope

Another important metrological aspect related to the microscopy measurements is the microscope resolving power that determines the accuracy of the spatial localization of the substances imaged. The resolving power determines the effective resolution of the microscope and is related to the minimum distance that two objects can have between each other to be still imaged as two single objects. Resolution of the microscope can be calculated theoretically using the Abbe's equation for the plane xy and along the z-axis:

$$d_{x,y} = \frac{\lambda}{2NA} = \frac{\lambda}{2(n\sin\theta)} \tag{40}$$

$$d_z = \frac{2\lambda}{NA^2} = \frac{2\lambda}{(n\sin\theta)^2} \tag{41}$$

These equations however in practice are oversimplified because between the objective lens and the sample the refractive index is hardly constant due to the sample or to the materials used like the coverslip, the immersion oil, the glass slid, etc.

Image formation in theoretical model is considered as a convolution with the sample of a fundamental unit called point spread function (PSF) that is the three-dimensional diffraction pattern generated by an infinitely small point source in the specimen and transmitted to the image plane through a high numerical aperture objective. The PSF generally has a round shape in the xy plane while along the z-axis has a more elongated shape due to a poorer resolution in the z axis. Generally the PSF sizes are considered as the resolution units of the microscope in the xy plane and along the z-axis.

In this doctorate thesis reference materials have been used to analyse the shape measured with different objective lenses configurations using forward CARS microscopy of polystyrene beads.

Polystyrene spheres with nominal size of 1 µm and 3 µm certified by NIST (SRM 1690 and SRM 1692) and 5 µm (Dynosphere SS-052-R by Dyno Particles AS) characterized using an AFM in our lab, have been used to characterize the laser scanning CARS microscope. The spheres have been dried on a quartz microscope slide that has been chosen to avoid Raman signal interferences and covered with a glass coverslip when oil immersion lens was used.

In order to focus the excitation beams an on the sample different objective lenses have been used in order to investigate also what is their influence on the measure.

Polystyrene spheres with nominal diameter of 1 µm and 3 µm have been measured focusing the excitation beams with 60x oil immersion lens (UPLSAPO 60XO NA=1.35, Olympus Europe), fully compensate for both spherical and chromatic aberrations from the UV to the near infrared region. The forward de-scanned CARS signal has been collected through an UPLSAPO 10x objective NA=0.4 (Olympus Europe) and focused on a PMT (model R3896, Hamamatsu). Bandpass filters centred at 716 nm with 43-nm bandwidth (FF01-716/43, Semrock), coupled with shortpass filters with 770nm of cut-off wavelength (FF01-770/SP, Semrock) are used before the detector to further block the residual excitation beams and transmit the CARS signal. In order to prevent sample damages and optimize the output signal the excitation beams were attenuated through a neutral density variable filter wheel (NDC-50C-4M, Thorlabs).

CARS signal intensity was measured in the range between 2940 cm^{-1} and 3135 cm^{-1} and the acquired spectrum is shown in Fig. 4.3. A maximum of CARS emission was measured at about 3047 cm^{-1}, which is consistent with the expected CARS signal computed previously for polystyrene.

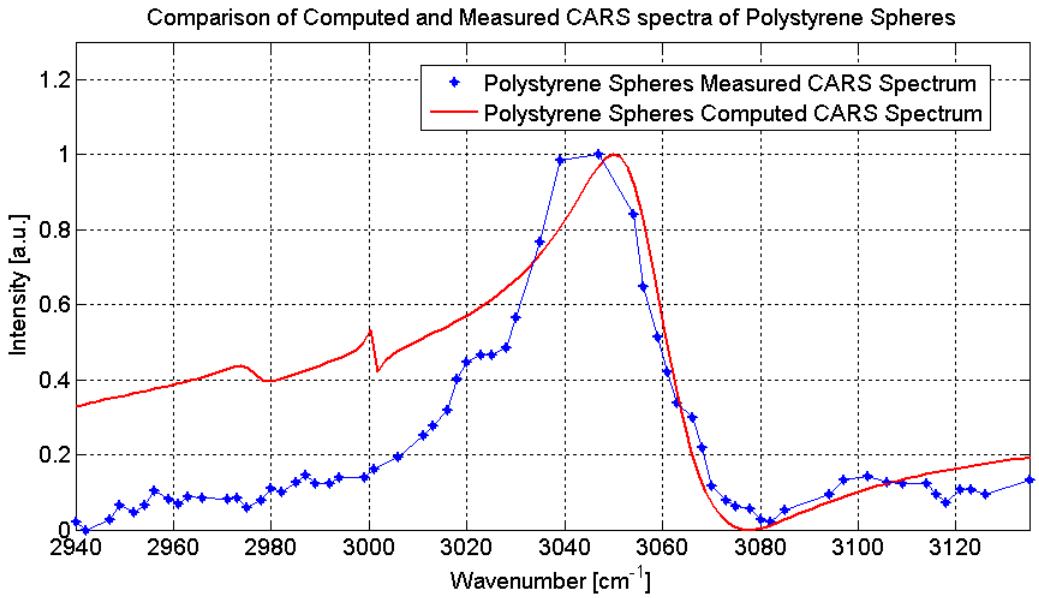

Fig. 4.3 (Blue dotted line) Measured CARS signal from polystyrene sphere using F-CARS. (Red line) Polystyrene computed CARS spectrum fitted to the measured one.

Figures 4.4A, 4.4B and 4.4C show SRM 1692 polystyrene spheres acquired at different ω_p - ω_s using the same detector setting (PMT voltage, offset and gain) to enhance the contrast for the first image and reduce the background contribution. When the OPO is tuned on the aromatic C-H stretching vibration at around 3047 cm^{-1} the spheres are clearly visible as it is shown in Fig. 4.4A. If the OPO is tuned at around 3018 cm^{-1} the spheres are still visible but less bright (Fig. 4.4B), while if the OPO is tuned to off-resonance condition at around 2940 cm^{-1} the spheres cannot be distinguished anymore from the background (Fig. 4.4C). This demonstrates the CARS chemical contrast and that actually CARS signal of polystyrene spheres is imaged.

The three-dimensional optical capability of microscope was characterized doing a Z stack imaging of the SRM 1690 and SRM 1692 polystyrene spheres, collecting images spaced respectively 0.2 µm and 0.3 µm on the Z-axis.

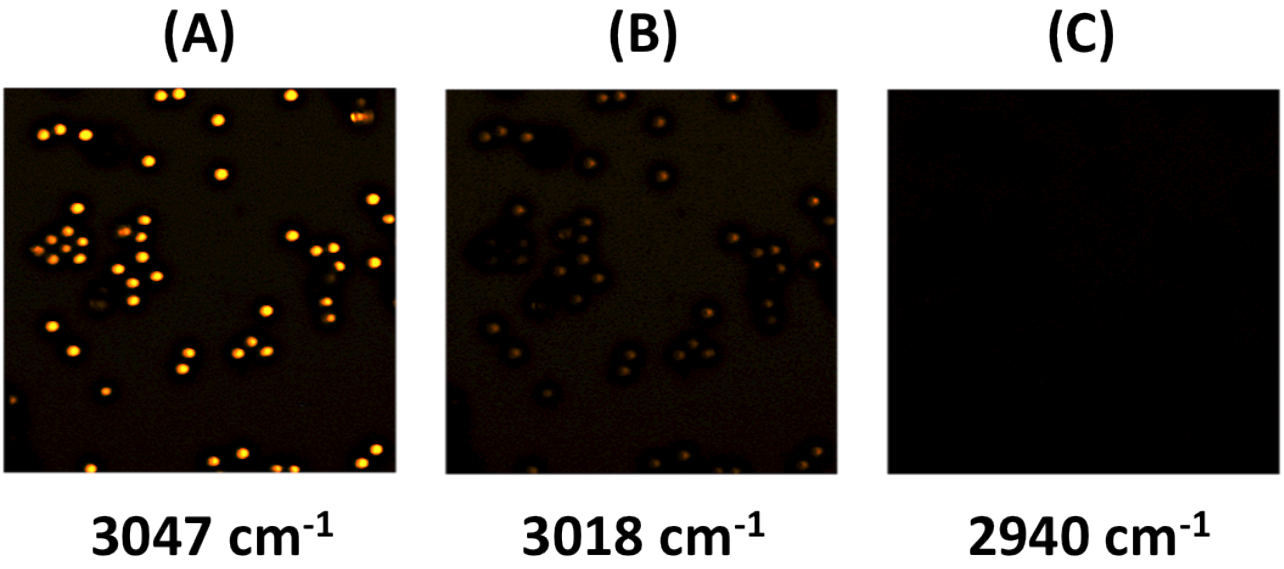

Fig. 4.4 (A) SRM 1692 polystyrene spheres CARS signal at 3047 cm^{-1}. (B) SRM 1692 polystyrene spheres CARS signal at 3018 cm^{-1}. (C) SRM 1692 polystyrene spheres CARS signal at 2940 cm^{-1}.

Figures 4.5A and 4.5B show the 3D visualizations (obtained with 3DViewer a free plug-in of the software ImageJ) of the polystyrene spheres with nominal diameter of 1 µm and 3 µm measured using forward CARS tuned at 3047 cm^{-1}. The 3D reconstructions of the spheres show a more elongated shape with respect to the real spherical shape.

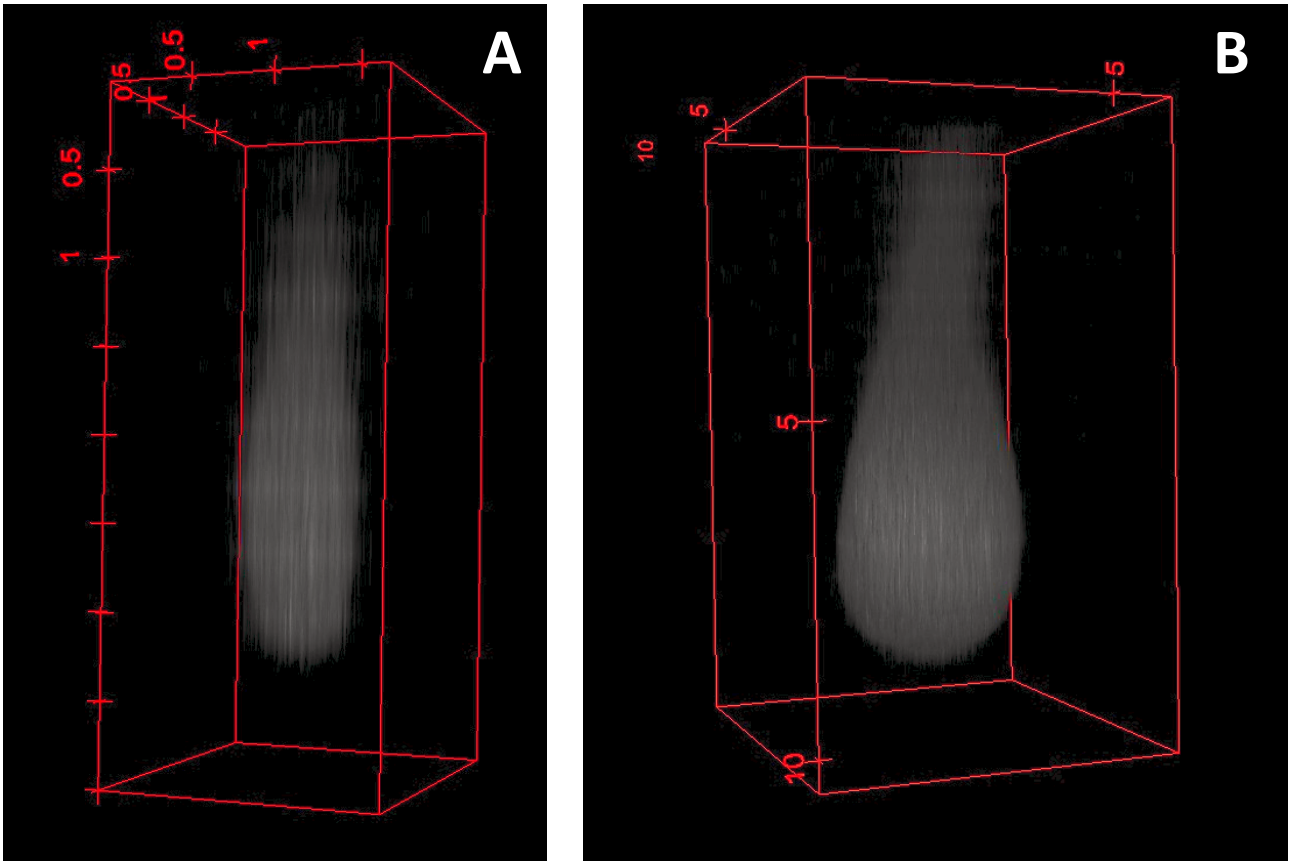

Fig. 4.5 shows a 3D visualization of 1 µm (A) and 3 µm (B) nominal diameters polystyrene sphere obtained with 3DViewer plug-in of the software ImageJ, using CARS microscopy.

Methods

Several methods have been used to measure the beads diameters and a metrological analysis has been done with respect to the image processing that has been used.

Both "manual" and automatic measurements of the beads diameters have been done starting from the acquired 3D image stacks.

The adopted "manual" measurement methods consist in:

- Determining with the help of ImageJ software the bead size selecting the XY and Z-plane sections that presented the largest bead images and analysing the intensity profile related to pixels under a line placed manually on centre of the bead images.
- Determining with the help of ImageJ software the bead size creating the XY and Z-plane maximum intensity projection sections, by drawing and measuring the geometrical properties of a reference line representing the visible extension of the object observed along the different sections.

The first “manual” measurement method puts in evidence how the measure is influenced by the choice of the intensity level that discriminates the object from the background, while the second method tries to overcome this limitation leaving the choice of where are the edges of the object to the user.

The adopted automatic measurements methods exploit an ImageJ plugin based on a specific algorithm that I developed in java language (see Appendix for the codes) and some of the tools present in the ImageJ software like Analyze Particles and AutoThreshold.

The specific algorithm that I developed (see Appendix - findDiameterAll_.java) finds the diameter of the equivalent circle that can describe with the minimum error the measured object shape. The algorithm process can be described with these consecutive steps:

- Loading of the 3D image stack of a single bead in the RAM memory together with the information related to the measure voxel size
- Searching among the images of the stack the slice with the higher average value of pixels intensity (assuming that this method can find one of the slices where the bead section is actually well displayed)
- Computing the threshold intensity value of the selected image using the Otsu’s method [74]
- Using the computed threshold value to create binary images for each image in the stack
- Filtering the obtained image selecting the object with the largest area (Fig. 4.6A)
- Computing the outline of the selected object for each slice (Fig. 4.6B)
- Computing the centres of mass of all the outlines for each slice
- Computing the equivalent circle diameter, calculating the average distance between the outline pixels and the centre of mass multiplied by two (Fig. 4.6C)
- Computing the standard deviation of the differences among the distances between the centre of mass and the real outline pixel positions with respect to the nearest circumference value, multiplied by two being referred to the circle diameter evaluation.
- Creating a results table with the list of computed diameters and related standard deviations for each stack image
- If no objects are present in the slice the computed diameter is displayed as zero

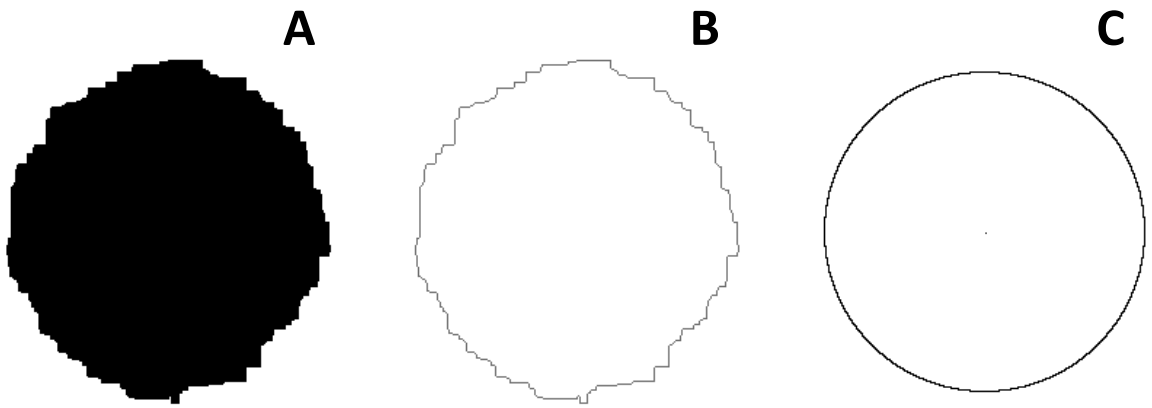

Fig. 4.6 Intermediate steps of the developed algorithm. (A) Binary image of the object filtered from "salt and pepper" noise. (B) Outline of the binary object. (C) Computed equivalent circumference of the object.

After processing the image stack with this algorithm, the image related to the slice with the largest diameter value is selected together with the maximum intensity projection section in the XY, ZX and ZY planes for further image processing, to evaluate the diameter using part of developed algorithm evaluating the equivalent diameter and other strategies through the *Analyze Particles* tool of ImageJ:

- Height and width of the boundary rectangle
- Major and minor axis of the equivalent computed ellipse
- Feret's statistical diameter [75]

The determination of the threshold value used to create the binary images is one of the main sources of uncertainty of the bead size measure. In fact the size measure is computed starting from a binary image that actually allows discriminating the measured object from the background.

The evaluation of the diameter using all the previously described strategies has been done imposing different threshold values in order to analyse the influence of this setup parameter in the diameter measurement.

In one case the imposed threshold values range between 5 and 250 with a step of 5, considering that for a 8 bit pixel image the intensity values are comprised between 0 and 255 (see Appendix - AnalyzeSingleAll_.java).

In the other case the imposed threshold values are computed using the main recognized methods already available in the AutoThreshold tool of the ImageJ software (see Appendix - findDiameterSingleAllthresMethods_.java).

These AutoThreshold methods are in total 17 and are based on a statistical evaluation of the threshold starting from the histogram of the population of the intensities among the pixels that compose the image and are obtained as follow [76, 77]:

- **Default:** this is the original method of auto thresholding available in ImageJ, which is a variation of the IsoData algorithm.
- **Huang:** implements Huang's fuzzy thresholding method. This uses Shannon's entropy function (one can also use Yager's entropy function) [78].
- **Intermodes:** this assumes a bimodal histogram. The histogram is iteratively smoothed using a running average of size 3, until there are only two local maxima: j and k. The threshold t is then computed as (j+k)/2. Images with histograms having extremely unequal peaks or a broad and flat valley are unsuitable for this method [79].
- **IsoData:** iterative procedure that divides the image into object and background by taking an initial threshold, then the averages of the pixels at or below the threshold and pixels above are computed. The averages of those two values are computed, the threshold is incremented and the process is repeated until the threshold is larger than the composite average [80].

  threshold = (average background + average objects)/2.
- **Li:** implements Li's Minimum Cross Entropy thresholding method based on the iterative version of the algorithm [81-83].
- **MaxEntropy:** implements Kapur-Sahoo-Wong (Maximum Entropy) thresholding method [84].
- **Mean:** uses the mean of grey levels as the threshold. It is used by some other methods as a first guess threshold [85].

- **MinError(I):** An iterative implementation of Kittler and Illingworth's Minimum Error thresholding. This implementation seems to converge more often than the original. Nevertheless, sometimes the algorithm does not converge to a solution. In that case a warning is reported to the log window and the result defaults to the initial estimate of the threshold that is computed using the Mean method [86].
- **Minimum:** similarly to the Intermodes method, this assumes a bimodal histogram. The histogram is iteratively smoothed using a running average of size 3, until there are only two local maxima. The threshold t is such that $y_{t-1} > y_t <= y_{t+1}$. Images with histograms having extremely unequal peaks or a broad and flat valley are unsuitable for this method [79].
- **Moments:** Tsai's method attempts to preserve the moments of the original image in the thresholded result [87].
- **Otsu:** Otsu's threshold clustering algorithm searches for the threshold that minimizes the intra-class variance, defined as a weighted sum of variances of the two classes [74].
- **Percentile:** assumes the fraction of foreground pixels to be 0.5 [88].
- **RenyiEntropy:** similar to the MaxEntropy method, but using Renyi's entropy instead [84].
- **Shanbhag:** implements Shanbhag's extenstion of the Kapur method, which includes a distance from the threshold in the entropy measure [89].
- **Triangle:** the triangle method constructs a line between the histogram peak and the farthest end of the histogram [90]. The threshold is the point of maximum distance between the line and the histogram. This implementation uses robust (default is 1% and 99%) estimation of histogram ends.
- **Yen:** implements thresholding based on a maximum correlation criterion [91, 83] as a more computationally efficient alternative to entropy measures.

Results and Discussion

The polystyrene spheres with nominal diameter of 1 µm and 3 µm have been analysed using the first "manual" measurement methods in order to evaluate the importance of the threshold level to define the boundary of the object measured.

The certified average particle diameter is (0.895 ± 0.008) µm for Standard Reference Material 1690 [92], while the certified number average diameter is (2.982 ± 0.016) µm for Standard Reference Material 1692 [93].

CARS imaging of a single polystyrene sphere with 1 µm nominal diameter is shown in the XY plane and ZY plane in Fig. 4.7A-4.7B. The intensity related to each pixel under a selecting line passing at the centre of the sphere it is extrapolated using ImageJ software. The diameter is measured computing the FWHM of the extrapolated intensity. From the XY plane image a FWHM of about 0.55 µm was measured while from the ZY plane image a FWHM of about 1.44 µm was measured.

In Fig 4.8A-4.8B CARS signal at around 3047 cm^{-1} of a single polystyrene sphere with 3 µm nominal diameter are shown and its size measured using ImageJ software. The intensity related to each pixel under a selecting line passing at the centre of the sphere it is extrapolated. The diameter is measured computing the FWHM of the extrapolated intensity. From the XY plane image a FWHM of about 2.88 µm was measured while from the ZY plane image a FWHM of about 3.34 µm was measured.

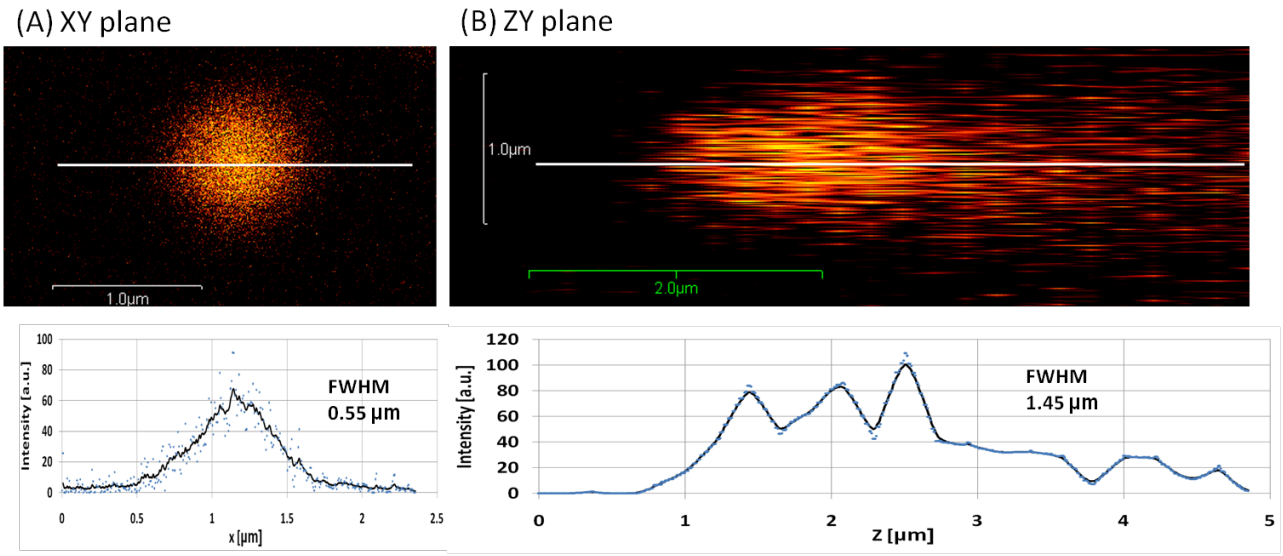

Fig. 4.7 (A) XY plane CARS imaging at 3047 cm^{-1} of SRM 1690 nominal 1 µm sphere. Under the image it is plotted the intensity vs X-axis related to the section covered by the white line. (B) ZY plane CARS imaging at 3047 cm^{-1} of SRM 1690 nominal 1 µm sphere. Under the image it is plotted the intensity vs Z-axis related to the section covered by the white line.

The obtained results do not fit with the certified ones, showing that the FWHM method typically used to define the resolution of the CARS technique is not sufficient to determine its measurement ability [28]. This is a well-known problem by the scientific community measuring size particles, since data analysis plays a significant role in the measurement together with the image quality.

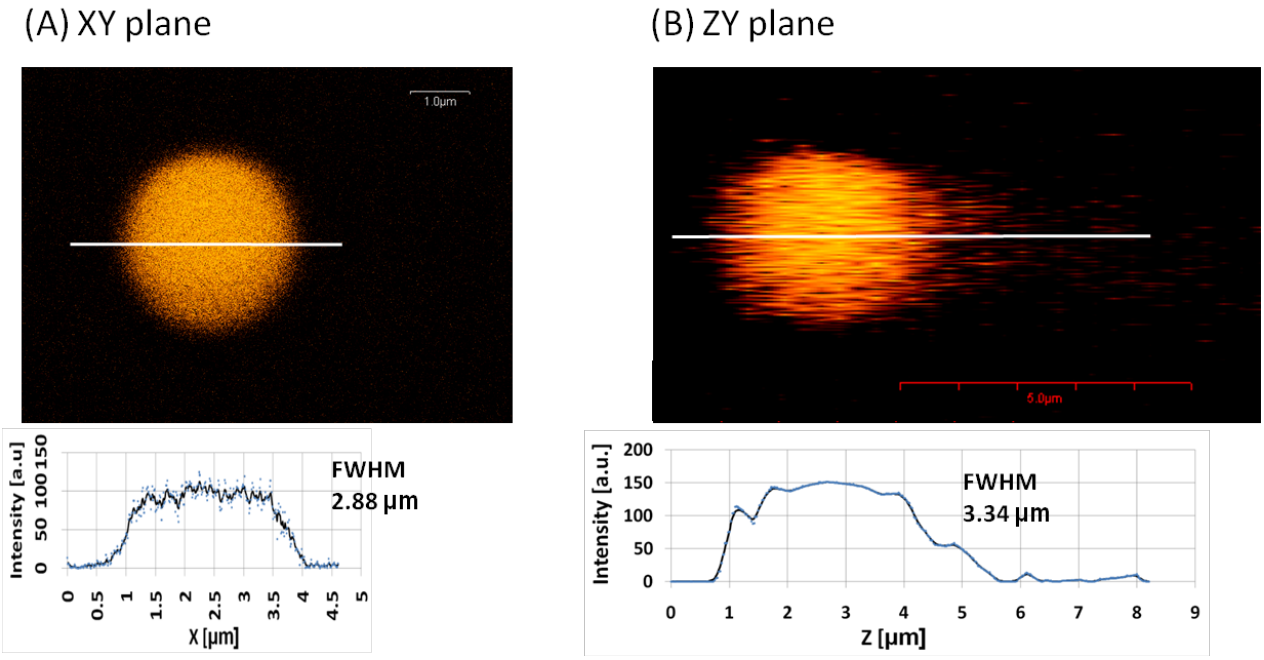

Fig. 4.8 (A) XY plane CARS imaging at 3047 cm^{-1} of SRM 1692 nominal 3 µm sphere. Under the image it is plotted the intensity vs X-axis related to the section covered by the white line. (B) ZY plane CARS imaging at 3047 cm^{-1} of SRM 1692 nominal 3 µm sphere. Under the image it is plotted the intensity vs Z-axis related to the section covered by the white line.

Watching to the intensity profiles related to the two spheres it is visible that the 1 µm nominal diameter sphere profile has a more disturbed shape than that referred to the 3 µm nominal diameter sphere. This is mainly due to a weaker signal arising from the smaller particle. The same effect can be evaluated looking at the histograms of the intensity distributions of the pixels composing the two images (Fig 4.9).

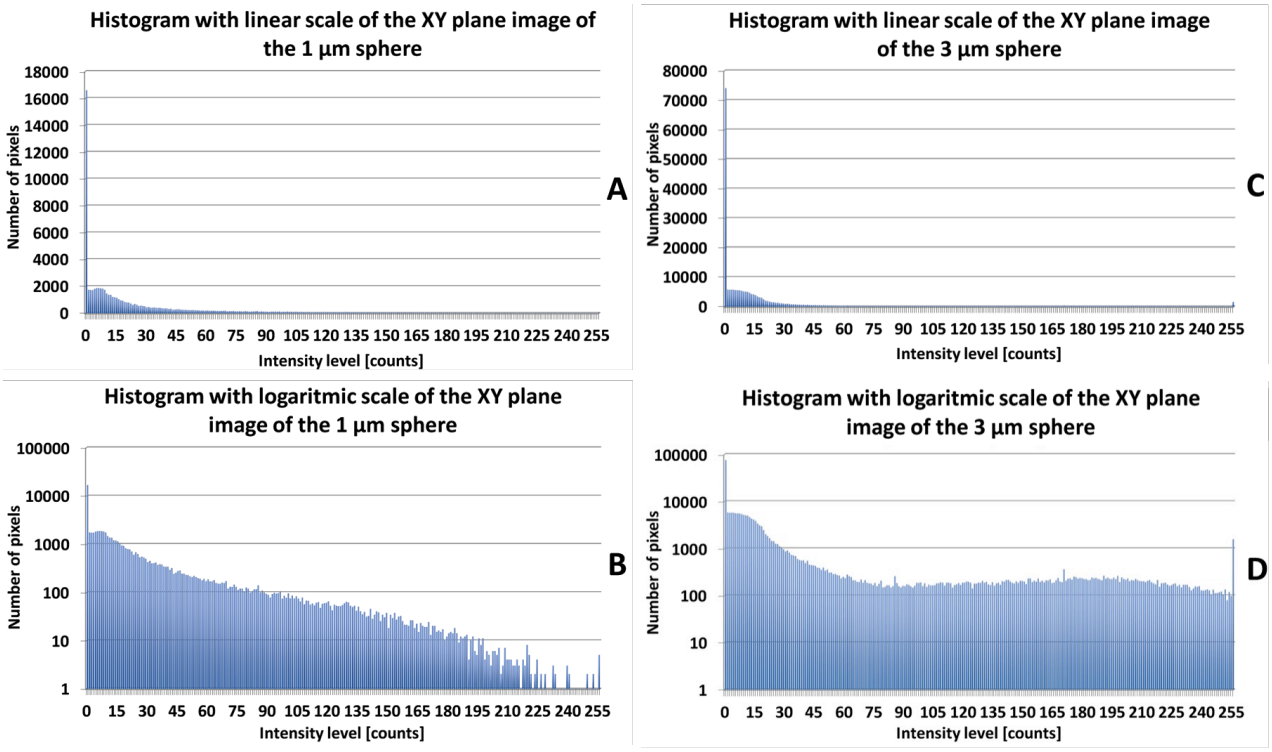

Fig. 4.9 Histogram of the pixels intensity distribution in linear and logaritmic scale related to the XY plane images of 1 µm sphere (A and B) and of 3 µm sphere (C and D).

The histogram related to the 1 µm diameter sphere shows a lower population of higher intensity pixels than the histogram related to the 3 µm diameter sphere. It is thus important to have a relevant population of higher intensity pixels because this helps to have a stronger discrimination between the background and the measured object.

The axial resolution of the CARS microscope was also studied using polystyrene beads with nominal diameter of 5 µm, characterized in our laboratory through atomic force microscopy (AFM) by Dr. E. Bernardi. A drop in which the spheres were present in solution has been dried on a glass slide. After evaporation of the solvent An AFM image of the sample was taken. The concentration was such that particles aggregated in regular domains, see Fig. 4.10.

In order to measure the average diameter of the beads, some topographic profiles were taken along the lines indicated in Fig. 4.10. An example of such a profile is presented in Fig. 4.10. The distance between the first and last peak profile was measured and then was divided by n-1, where n is the number of peaks in the profile. This procedure was repeated for the six profiles. The average beads diameter was found to be (4,983 ± 0.0075) µm, in this expression the uncertainty is given by the standard deviation of the values resulting from the different profiles.

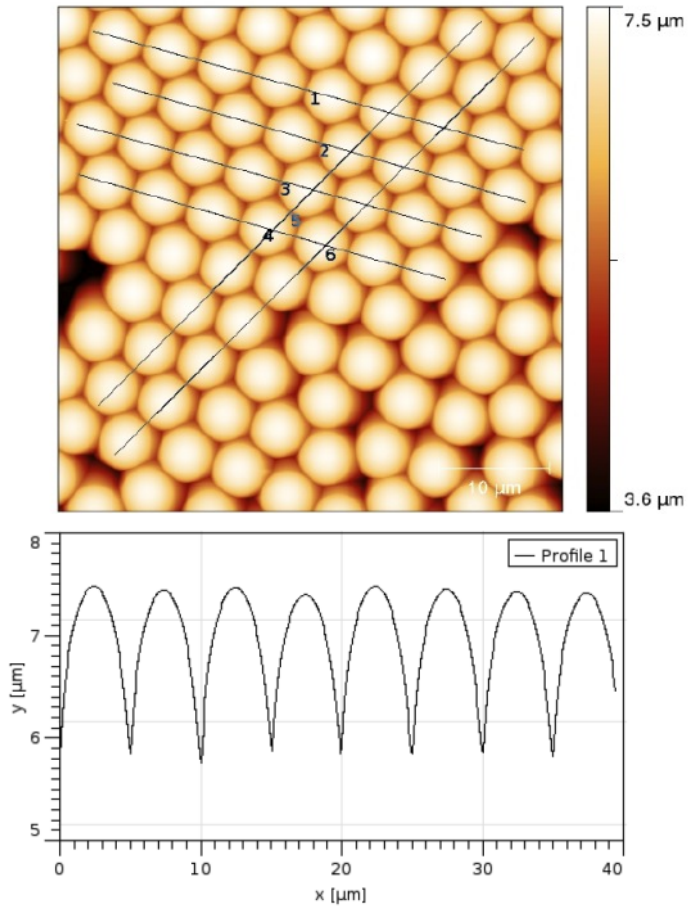

Fig. 4.10 (Top) AFM imaging of Dynosphere 5 µm polystyrene beads. (Bottom) heights profile referred to one of the lines traced on the AFM topographic image.

Polystyrene spheres with nominal diameter of 5 µm have been measured using two different focusing objective lens and condenser lens configurations, in order to evaluate also this parameter of influence. One configuration using a 20x lens (UPLSAPO 20x NA=0.75, Olympus Europe) as a focusing lens and collecting the forward de-scanned CARS signal through a 4x lens (UPLSAPO 4x NA=0.16, Olympus Europe), the other focusing the excitation beams with a 10x lens (UPLSAPO 10x NA=0.4, Olympus Europe) and collecting the forward de-scanned CARS signal through a 4x lens (UPLSAPO 4x NA=0.16, Olympus Europe). Bandpass filters centred at 716 nm with 43-nm bandwidth (FF01-716/43, Semrock), coupled with shortpass filters with 770nm of cut-off wavelength (FF01-770/SP, Semrock) are used before the detector to further block the residual excitation beams and transmit the CARS signal. The forward de-scanned CARS signal was then focused on a PMT (model R3896, Hamamatsu). In order to prevent sample damages and optimize the output signal the excitation beams were attenuated through a neutral density variable filter wheel (NDC-50C-4M, Thorlabs).

A 3D imaging of the 5 µm nominal diameter beads has been done using a Z-step of 0.5 µm with both configuration setup of the focusing objective lens and the condenser lens. The acquired 3D image stacks have been analysed and a dimensional characterization of the measured beads has been done using the second “manual” measurement method.

The dimensional characteristics of the obtained shapes were measured along the different axis using their axial projections. The projections along the different axis were obtained by using the "Maximum Intensity

Projection" tool of ImageJ software, creating an image where each pixel have the maximum intensity level of the corresponding pixel between all the section images along the axis of reference.

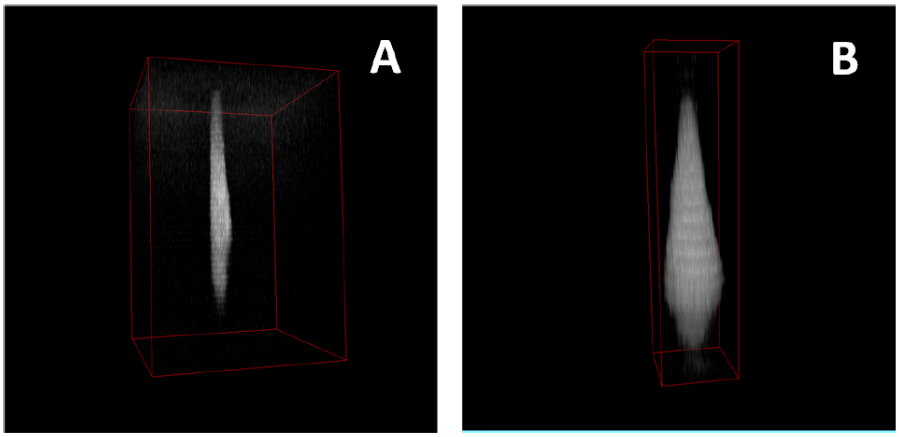

Fig. 4.11 3D visualization of 5 µm nominal diameter sphere obtained with ImageJ 3DViewer plug-in, using CARS microscopy with two different lenses configurations.

The dimensions were measured manually by drawing a reference line (in red in Fig. 4.12 and 4.13) that represents the visible extension of the object observed along the different sections. The table 4.1 shows the results of dimensional measurements of polystyrene spheres with nominal diameter of 5 µm, along the different spatial sections obtained using two different pairs of lenses. Using the configuration with 20x excitation and 4x detection objectives, the measurement results show a resolving power greater than the configuration with 10x excitation and 4x detection objectives.

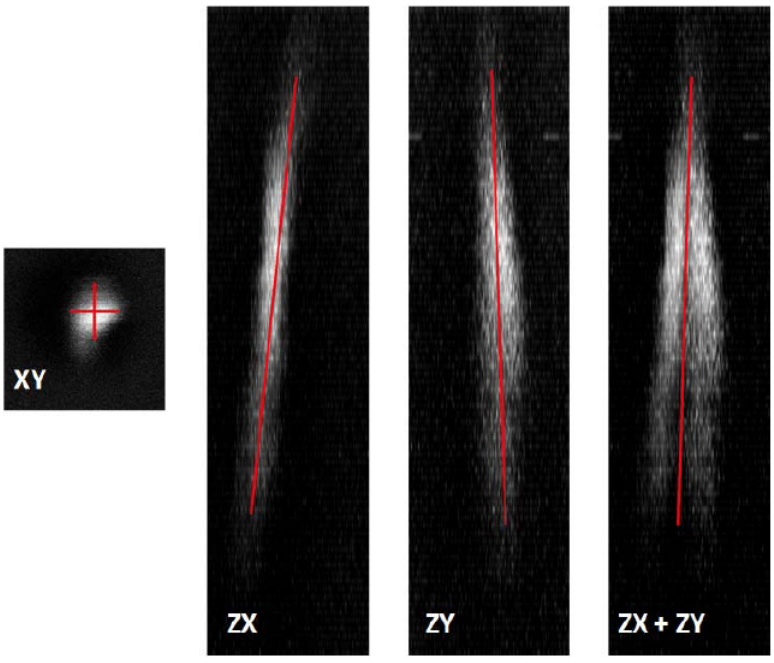

Fig. 4.12 Maximum intensity projections of different sections of a 5 µm nominal diameter sphere using a 10x excitation objective and a 4x collection objective. In red are traced the references of the sizes measures. (XY) Spatial projection of the XY section along the Z-axis; (ZX) Spatial projection of the section ZX along the Y-axis; (ZY) Spatial projection of the section ZY along the X-axis; (ZX+ZY) Sum of the ZX and ZY spatial projections.

In both cases the dimensional results related to XY section are slightly underestimated while those related to sections along the z-axis are greatly overstated. This experiment shows that while the measures referred to XY plane have a relatively low uncertainty, those related to the Z-plane have a systematic error of overestimation. The angle measure gives an idea of the astigmatism of the optical system, and then how the two lenses are not perfectly aligned with each other with respect to the optical axis of propagation.

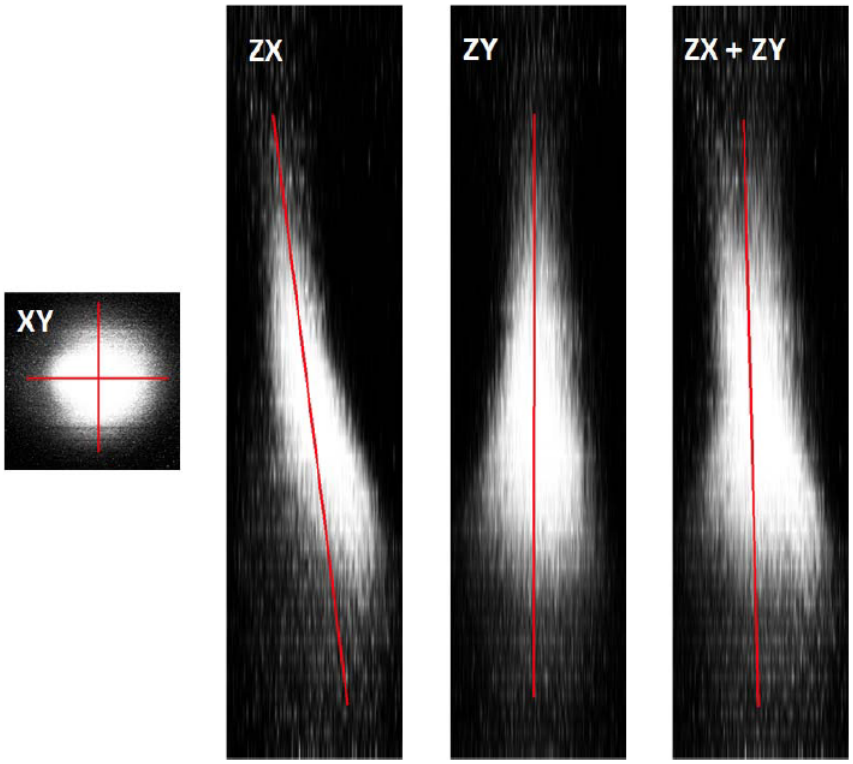

Fig. 4.13 Maximum intensity projections of different sections of a 5 µm nominal diameter sphere using a 20x excitation objective and a 4x collection objective. In red are traced the references of the sizes measures. (XY) Spatial projection of the XY section along the Z-axis; (ZX) Spatial projection of the section ZX along the Y-axis; (ZY) Spatial projection of the section ZY along the X-axis; (ZX+ZY) Sum of the ZX and ZY spatial projections.

The results in the table 4.1 show that using the 10x lens as excitation objective configuration setup, the measures of the bead diameter in the Z-axis have values that are about 1.7 times of those obtained using the 20x lens as excitation objective. It is also interesting to observe that this value is close to the ratio between the numerical apertures of the two objective lenses that values 1.875.

	Excitation objective 10x NA=0.4 Collection objective 4x NA=0.16		Excitation objective 20x NA=0.75 Collection objective 4x NA=0.16		Ratio
Label	Length [µm]	Angle	Length [µm]	Angle	
Projection XY	3.66	0°	4.05	0°	0.9
Projection XY	3.13	90°	3.84	90°	0.81
Projection ZX	27.71	5.88°	16.17	-7.23°	1.66
Projection ZY	28.73	-1.78°	15.85	0.06°	1.81
Projection	28.31	1.7°	16	-1.44°	1.77

Table 4.1 Table of the manual measurements results referred to the 5 µm nominal sphere using the two lenses configurations.

If eq. (41) is used to compute the theoretical axial resolution substituting to the squared numerical aperture NA^2, the product between the two coupled lens NA_{ex} and NA_{col}: